Macedonian Journal of Chemistry and Chemical Engineering, Vol. **45**, No. 1, pp. xx–xx (2026)

MJCCA9 –

ISSN 1857-5552
e-ISSN 1857-5625

Received: May 20, 2026
Accepted: June 8, 2026

DOI: 10.20450/mjcce.2026.3562
Original scientific paper

MICROWAVE-ASSISTED GREEN FABRICATION OF NICKEL FOAM–REDUCED GRAPHENE OXIDE–NICKEL SULFIDE NANOCOMPOSITE: STRUCTURAL, SPECTROSCOPIC, AND ELECTROCHEMICAL PERFORMANCE EVALUATION FOR SUPERCAPACITOR APPLICATIONS

Prabaharan Panchanathan[1,2], Maadathi Sivakumar[2], Gunasekaran Marudhai[3], Brindha Ganesan[4], Sivasankari Gnanam[2*], Boobalan Sivalingam[5], Devi Selvaraj[2]

[1] *Department of Chemistry, Government Polytechnic College Tiruchirappalli– 620 022, India*
[2] *Department of Chemistry, Cauvery College for Women (A), Tiruchirappalli – 620 018, India, Affiliated to Bharathidasan University*
[3] *Department of Chemistry, J J College of Engineering and Technology, Tiruchirappalli – 620 009, India*
[4] *Department of Chemistry, V.S.B. Engineering College Autonomous, Karur – 639 111, India.*
[5] *Department of Chemistry, Indra Ganesan College of Engineering, Manikandam, Tiruchirappalli – 620012*

gsivasankari.chem@cauverycollege.ac.in

A microwave-assisted green synthesis route was employed to fabricate a nickel foam–reduced graphene oxide–nickel(II) sulfide (Ni foam–rGO–NiS) nanocomposite using *Coccinia grandis* leaf extract as the bio-reducing and stabilizing agent for supercapacitor applications. The Ultraviolet – Visible (UV) spectrum revealed an absorption peak of 239 nm (rGO) and 313 nm (NiS), confirming the formation of a composite that facilitates efficient electron transfer between the two components, potentially reducing the band gap energy. Fourier Transform Infrared spectra (FTIR) confirmed successful loading of NiS nanoparticles onto rGO, with associated phytochemical functional groups acting as reducing, capping, and stabilizing agents. X-ray Diffraction (XRD) patterns validated formation of hexagonal NiS and reduction in the sheet structure of rGO, thereby elucidating the nature of the nanocomposite. The average crystallite size, estimated using the Debye–Scherrer equation, was approximately 2–5 nm (NiS) and approximately 30.4 nm (rGO). The surface morphology of the nanocomposite displayed an exfoliated wrinkled sheet structure, with NiS particles uniformly dispersed throughout. Elemental analysis verified that the material had achieved the expected purity levels, with no detectable impurities, while the Dynamic Light Scattering (DLS) indicated a particle size of approximately 100 nm in solution. The Ni foam–rGO–NiS electrode demonstrated significantly enhanced electrochemical performance. Cyclic voltammetry conducted at the same scan rate revealed intense redox peaks, thus confirming pseudocapacitive behavior. Electrochemical impedance spectroscopy (EIS) indicated low charge-transfer resistance with high electrochemical activity. This electrode achieved a high specific capacitance of approximately 633.3 F g^{-1} at 1 A g^{-1} and approximately 422.2 F g^{-1} at 5 A g^{-1}, as well as exhibiting good rate capability and cycling stability, with 80–85 % capacitance retention over 3000 cycles. The synergistic combination of highly conductive rGO, redox-active NiS, and porous Ni foam enhanced charge storage and transportation. The prepared green-synthesized, reduced graphene oxide–nickel(II) sulfide nanocomposite is proposed as a promising electrode nanomaterial for supercapacitor applications.

Keywords: green synthesis; nickel sulfide nanoparticles; reduced graphene oxide nanocomposite; *Coccinia grandis* leaf extract; supercapacitor electrode materials

МИКРОБРАНОВО ПОТПОМОГНАТО ЗЕЛЕНО ДОБИВАЊЕ НА НАНОКОМПОЗИТ ОД НИКЕЛСКА ПЕНА – РЕДУЦИРАН ГРАФЕН ОКСИД – НИКЕЛ(II) СУЛФИД: СТРУКТУРНА, СПЕКТРОСКОПСКА И ЕЛЕКТРОХЕМИСКА ЕВАЛУАЦИЈА НА ПЕРФОРМАНСИТЕ ЗА ПРИМЕНА ВО СУПЕРКОНДЕНЗАТОРИ

За изработка на нанокомпозит од никелска пена – редуциран графен оксид – никел(II) сулфид (Ni пена–rGO–NiS) беше применет микробраново потпомогнат зелен синтетички пристап, користејќи екстракт од листови на *Coccinia grandis* како биоредуцирачко и стабилизирачко средство за примена во суперкондензатори. Ултравиолетово-видливиот (UV-Vis) спектар покажа апсорпциски пик на 239 nm (rGO) и 313 nm (NiS), потврдувајќи формирање на композит кој овозможува ефикасен пренос на електрони помеѓу двете компоненти, со потенцијално намалување на енергијата на забранетата зона (band gap). Фурјетрансформациска инфрацрвена спектроскопија (FTIR) потврди успешно нанесување на NiS наночестички врз rGO, при што придружните фитохемиски функционални групи дејствуваат како редуцирачки, капирачки и стабилизирачки средства. Рендгенската дифракција (XRD) го потврди формирањето на хексагонален NiS и редукцијата на слоевитата структура на rGO, со што се разјаснува природата на нанокомпозитот. Просечната големина на кристалитите, проценета со равенката на Дебај–Шерер, изнесуваше приближно 2–5 nm за NiS и околу 30,4 nm за rGO. Површинската морфологија на нанокомпозитот покажа ексфолирана набрана слоевита структура, при што честичките на NiS беа рамномерно дисперзирани низ целата површина. Елементната анализа потврди дека материјалот ја постигнал очекуваната чистота без детектирани нечистотии, додека динамичкото расејување на светлина (DLS) укажа на големина на честички од приближно 100 nm во раствор. Електродата од Ni пена–rGO–NiS покажа значително подобрени електрохемиски перформанси. Цикличната волтаметрија, изведена при иста брзина на скенирање, откри изразени редокс-пикови, со што се потврди псевдокапацитивното однесување. Електрохемиската импедансна спектроскопија (EIS) укажа на ниска отпорност при пренос на полнеж и висока електрохемиска активност. Оваа електрода постигна висока специфична капацитивност од приближно 633,3 F g^{-1} при 1 A g^{-1} и приближно 422,2 F g^{-1} при 5 A g^{-1}, при што покажа добра способност за работа при различни густини на струја и добра циклична стабилност, со задржување на 80–85 % од капацитивноста по 3000 циклуси. Синергетската комбинација од високо проводлив rGO, редокс-активен NiS и порозна никелска пена го подобри складирањето и транспортот на полнежот. Подготвениот со зелена синтеза нанокомпозит од редуциран графен оксид и никел(II) сулфид се предлага како перспективен електроден наноматеријал за примена во суперкондензатори.

Клучни зборови: зелена синтеза; наночестички од никел сулфид; нанокомпозит од редуциран графен оксид; екстракт од листови на *Coccinia grandis*; електродни материјали за суперкондензатори.

1. INTRODUCTION

The growing global energy demand, coupled with the depletion of traditional fossil fuels and environmental concerns, has driven intensified re-search efforts focused on developing sustainable, high-performance energy storage systems.[1,2] Among these technologies, supercapacitors have garnered significant attention in recent years due to their high power density, rapid charge–discharge capabilities, and long cycle life.[3–5] Nevertheless, their relatively low energy density compared to conventional batteries remains a critical limitation, driving extensive research into electrochemically optimized electrode materials.[6–8]

Supercapacitors are typically divided into two distinct types: electric double–layer capacitors (EDLCs) and pseudocapacitors, based on their charge storage mechanisms.[1,9,10] EDLCs store charge via a layer of electrostatically adsorbed ions at the electrode/electrolyte interface without any charge transfer, demonstrating extremely high cycling stability but low capacitance.[9] In contrast, pseudocapacitors store charge through rapid and reversible electron transfer via one-electron redox intercalation reactions, and thus exhibit extremely high capacitance.[11] Recent research efforts in supercapacitor development have focused on optimizing the performance of hybrid materials that combine both charge storage mechanisms.[12]

Carbon-based materials, including graphene and its derivatives (e.g., reduced graphene oxide (rGO)), are most frequently utilized as electrodes in EDLCs owing to their large specific surface area, high electrical conductivity, and excellent mechanical strength.[13] Nevertheless, the pseudocapacitance of rGO remains limited due to its inherently low intrinsic pseudocapacitive activity.[14] One effective strategy to address this limitation involves incorpora-ting re-

dox-active materials into the carbon matrix, thereby enhancing both capacitance and energy density.[15]

Transition metal-based oxides, hydroxides, and sulfides, as pseudocapacitive materials, have been extensively investigated due to the availability of multiple valence states and numerous redox-active sites.[16] Transition metal sulfides (TMS), as a subclass of transition metal chalcogenides, are particularly promising because of their higher electrical conductivity and electrochemical activity compared with their oxide counterparts.[17] However, their performance remains constrained by particle agglomeration, relatively poor cycling stability, and inadequate electrical conductivity in their pristine state.[18]

Hybrid nanocomposites that combine metal compounds with conductive carbon matrices have been widely employed to mitigate the aforementioned limitations. The carbon framework functions as a conductive host, facilitating electron transfer and providing an electrochemically accessible high surface area for the uniform dispersion of electroactive materials, whereas the metal compounds primarily contribute to faradaic charge storage. This synergistic interaction results in the superior electrochemical performance of hybrid materials.[19]

Additionally, researchers are increasingly adopting more eco-friendly synthesis routes. Conventional chemical synthesis approaches, which rely on toxic reagents and energy-intensive processes, pose significant sustainability challenges. As an alternative, green synthesis methods utilizing plant extracts have been developed; in these methods, phytochemicals naturally present in the plants serve as reducing, stabilizing, and capping agents during nanomaterials synthesis.[20] Given the diversity of plant sources, *Coccinia grandis*, a species rich in phytochemicals including flavonoids, polyphenols, and alkaloids, offers potential as a reducing and capping agent for the production of stabilized nanomaterials.[21]

Although several rGO–metal sulfide-based supercapacitor systems have previously been reported, most synthesis approaches still rely on hydrothermal processing, toxic chemical reducing agents, or energy-intensive methods.[18] Furthermore, plant-mediated synthesis of NiS–rGO hybrid electrodes directly integrated with porous Ni foam "current collectors" remains comparatively underexplored. Consequently, the development of a rapid, eco-friendly, and scalable fabrication strategy for achieving highly dispersed NiS nanoparticles on conductive graphene frameworks represents an important scientific advancement.

In this study, a microwave-assisted green synthesis route employing *C. grandis* leaf extract was utilized for the fabrication of an rGO–NiS nanocomposite electrode. The phytochemicals present in *C. grandis*, including flavonoids, polyphenols, and alkaloids, serve as multifunctional agents, acting simultaneously as reducing, stabilizing, and capping agents during nanoparticle formation.[20] These bioactive compounds effectively prevent nanoparticle agglomeration, enhance the uniform dispersion of NiS on rGO sheets, and strengthen interfacial interactions between the conductive carbon framework and the electroactive NiS nanoparticles.

The novelty of this study lies in the integration of (i) microwave-assisted rapid synthesis, (ii) bio-mediated stabilization using *C. grandis* leaf extract, and (iii) synergistic integration of rGO, NiS, and porous Ni foam into a single electroactive architecture for supercapacitor applications. The resulting electrode exhibited enhanced charge transport, ion diffusion, and pseudocapacitive electrochemical behavior.

2. EXPERIMENTAL SECTION

2.1. *Materials*

Nickel nitrate hexahydrate (Ni(NO)·6HO), sodium sulfide (NaS), Potassium hydroxide (KOH), ethanol and reduced graphene oxide (rGO) were used in this study. All chemicals were purchased from Sigma-Aldrich (St. Louis, MO, USA) and used without further purification. Distilled water was used throughout all experimental procedures.

Fresh leaves of Coccinia grandis were collected from naturally growing plants in a private agricultural field in Tiruchirappalli, Tamil Nadu, India, and used for the preparation of the plant extract.

2.2. *Preparation of Coccinia grandis leaf extract*

Fresh leaves of *Coccinia grandis* were rinsed thoroughly with distilled water to remove dust and other impurities. The leaves were then shade-dried at room temperature and ground into a fine powder. Subsequently, 10 g of the dried leaf powder was added to 100 mL of distilled water and immersed in a water bath (LB-WBS12, Labcare Instruments, India) at 70–80 °C for 30 min to extract the phytochemicals. The solution was cooled to room temperature and filtered using Whatman Grade 1 filter paper (Cytiva, United Kingdom) thereby removing solid residues from the solution. The resulting filtrate (green) was stored at 4 °C and functioned as a natural reductant and capping agent during the synthesis of nanoparticles (Fig. 1).[20]

Fig. 1. Schematic representation of *Coccinia grandis* leaf extraction

2.3. *Microwave-assisted green synthesis of nickel sulfide nanoparticles*

Nickel sulfide nanoparticles were synthesized via a microwave-assisted synthesis procedure. To prepare the precursor solution, an amount of 0.1 M nickel(II) nitrate solution was dissolved in distilled water to obtain a solution of uniform composition. Fresh leaf extract of *C. grandis* was added dropwise to the solution under constant magnetic stirring. Subsequently, a 0.1 M aqueous sodium sulfide solution was introduced dropwise as the sulfur source to initiate the synthesis of NiS nanoparticles. The mixture was stirred for 30 min. The resulting solution was then irradiated with microwave (20SC2, IFB Industries Ltd., India) radiation for 9 min to allow rapid nucleation and growth of nickel sulfide nanoparticles. Microwave-assisted synthesis provided constant heating and shortened reaction times. Following microwave treatment, a dark precipitate formed, confirming the growth of NiS nanopowder. The dark precipitate was removed by centrifugation (C-854/8, REMI, India) and washed repeatedly with deionized water and ethanol to purify the nanopowder. Finally, it was dried in hot-air oven (TI-125-B, Tempo Instruments Pvt. Ltd., India) at 80 °C for 12 hrs. (Fig. 2).[22]

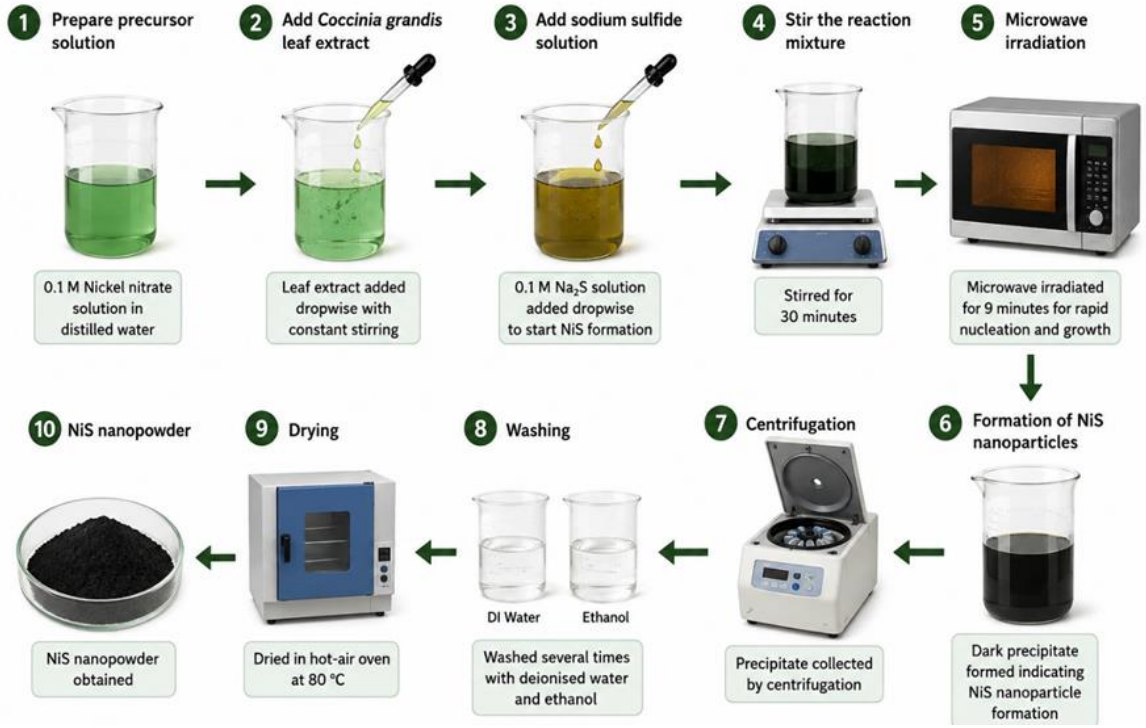

Fig.2. Schematic representation of NiS nanoparticle synthesis using *Coccinia grandis* leaf extraction

2.4. *Preparation of rGO–NiS nanocomposite*

The rGO–NiS nanocomposite was prepared using a simple dispersion method. One gram of NiS nanoparticles, which had been synthesized previously, was dispersed in distilled water and ultra-sonicated (LMUC-2, Labman Scientific Instruments, India) for 30 min. Commercial rGO was also dispersed in distilled water to ensure optimal dispersion of the sheets. The NiS suspension was then gradually added to the suspended rGO under magnetic stirring. The mixture was stirred and heated gently for 4 h to allow uniform anchoring of NiS nanoparticles onto the rGO sheets. The obtained rGO–NiS nanocomposite was collected by centrifugation, washed with distilled water and ethanol, and then dried at 60 °C to yield the final nanocomposite powder (Fig. 3).

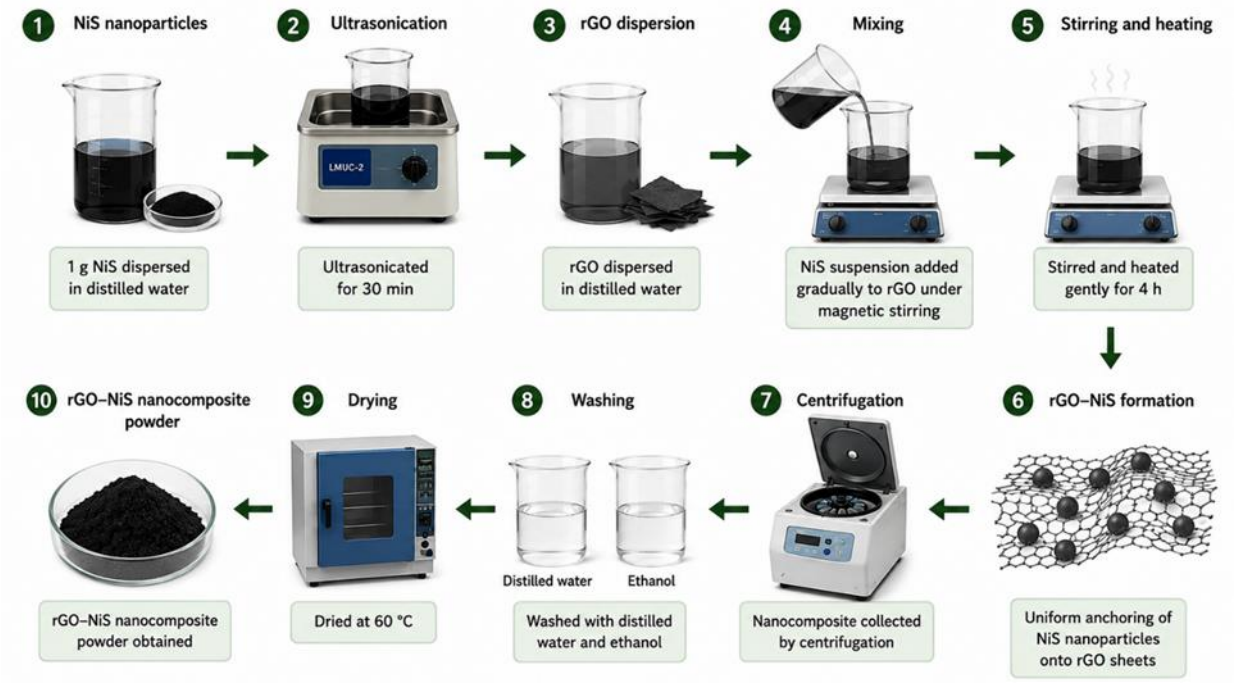

Fig. 3. Schematic representation of rGO–NiS nanocomposite preparation

2.5. *Characterization techniques*

Various analytical techniques were employed to characterize the prepared materials. UV–Vis spectroscopy (Lambda 365, PerkinElmer, USA) was carried out in the wavelength range of 200–800 nm to assess the optical properties of the samples. Fourier transform infrared (Spectrum Two, PerkinElmer, USA) Spectroscopy was performed in transmission mode using the KBr pellet method in the wavenumber range of 4000–400 cm^{-1} for functional group identification and to investigate the interaction of NiS nanoparticles with biomolecules derived from the C. grandis leaf extract. X-ray diffraction (X'Pert³ Powder, Malvern Panalytical, The Netherlands) as performed using Cu Kα radiation (λ = 1.5406 Å) for phase and crystalline structure identification. DLS (NanoPlus, Micromeritics, USA). were conducted to determine particle size distribution and colloidal stability. Scanning electron microscopy (SEM) (Vega 3, TESCAN, Czech Republic) and energy-dispersive X-ray spectroscopy (EDX) (EDX, Bruker, Germany) were utilized for surface and particle imaging, as well as for confirmation of elemental composition.

2.6. *Electrochemical measurements*

Electrochemical tests were conducted in a standard three-electrode configuration. The working electrode was fabricated by depositing the prepared rGO–NiS coating onto nickel foam. Platinum wire and Ag/AgCl served as the counter and reference electrode, respectively, immersed in aqueous KOH. The recorded electrochemical behaviors were analyzed (CHI 660E, CH Instruments, USA) at various scan rates within the same potential window using cyclic voltammetry (CV), Chronocoulometry (CC) measurements were carried out to investigate the charge storage characteristics of the prepared electrodes, and utilizing different galvanostatic charge–discharge (GCD) tests to calculate the specific capacitance:

$$C = \frac{I\Delta t}{m\Delta V} \quad (1)$$

where C is the specific capacitance (F g^{-1}), I is the discharge current (A), Δt is the discharge time (s), m is the mass of active material (g), and ΔV is the potential window (V).

Electrochemical Impedance Spectroscopy (EIS) (CHI 660E, CH Instruments, USA) was employed across a broad spectrum of frequencies to investigate charge-transfer resistance and ion-diffusion characteristics, with the findings visualized using Nyquist plots. The electrochemical measurements were replicated under identical experimental conditions using 0.1 M KOH electrolyte. Cyclic voltammetry (CV) measurements were carried out in the potential window of −0.4 to 0.5 V, galvanostatic charge–discharge (GCD) measurements were performed in the potential range of 0 to 0.5 V at current densities ranging from 1 to 5 A g^{-1}, and electrochemical impedance spectroscopy (EIS) measurements were recorded over a frequency range of 100 kHz to 1 Hz. These measurements were repeated to verify the reproducibility of the obtained electrochemical results. The observed trends in capacitance behavior and electrochemical response were determined to be consistent within experimental variation.

3. RESULTS AND DISCUSSION

3.1. *UV–Visible Spectroscopy Analysis*

The UV–Vis absorbance spectra recorded in Figures 4a and 4b were used to evaluate the optical properties of rGO and the rGO–NiS nanocomposite, respectively. For consistency in comparison, the UV–Vis spectra were normalized with respect to the highest absorbance intensity of the rGO spectrum. In Figure 4a, rGO displayed a strong absorption peak at approximately 239 nm, which was assigned to the π→π* transition of C=C bonds and demonstrated restoration of the sp^2 carbon network after reduction.[15] In Figure 4b, the rGO–NiS nanocomposite retained the absorption peak near 239 nm, validating the presence of rGO in the composite. An additional absorption feature was observed around 313 nm and linked to charge-transfer-related transitions of NiS nanoparticles. The broader absorption profile observed for the rGO–NiS nanocomposite relative to rGO suggested interaction between NiS nanoparticles and rGO sheets, indicating the successful formation of the composite material.

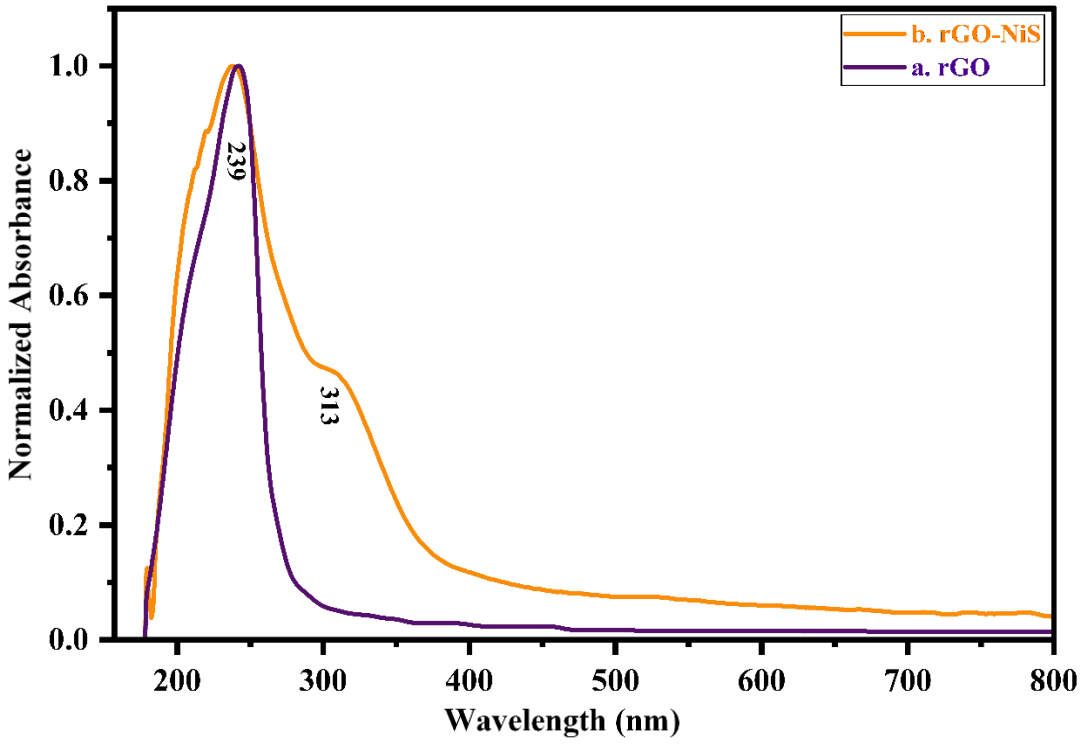

Fig. 4. Normalized UV–Vis absorption spectra of (a) rGO and (b) rGO–NiS nanocomposite recorded in the wavelength range of 200–800 nm

3.2. *FTIR spectral analysis*

The functional groups present in the as-prepared rGO and rGO–NiS composite, synthesized using *C. grandis* leaf extract, were analyzed via FTIR spectroscopy. In the FTIR spectrum of rGO (Fig. 5a), the bands at approximately 490, 860, 986, 1476, and 3478 cm^{-1} indicated the presence of various residual oxygen-containing functional groups [23] alongside the graphitic vibrations. Specifically, this broad band at approximately 3478 cm^{-1} was attributed to the O–H stretching vibrations, suggesting the possible existence of hydroxyl groups or physically adsorbed moisture. The band at approximately 1476 cm^{-1} corresponded to the skeletal vibrations of the C=C groups within the graphite structure, demonstrating some degree of restoration of the sp^2 network following reduction. The bands at approximately 860 and 986 cm^{-1} were linked to the C–H vibrational bending modes of peripheral groups, whereas the high-intensity band at approximately 490 cm^{-1} was associated with C–O vibrations or lattice deformation, further indicating the presence of residual oxygen-containing functionalities.

The FTIR spectrum of the rGO–NiS nanocomposite (Fig. 5b) displayed intense bands at approximately 756, 1680, 2120, and 3500 cm^{-1}. The band observed at approximately 756 cm^{-1} was attributed to Ni–S stretching vibrations, indicating the successful formation of nickel sulfide nanoparticles on the rGO. The peak at approximately 1680 cm^{-1} was assigned to C=O stretching modes or conjugated C=C stretching vibrations, which suggested the interaction of NiS with the rGO framework. The peak at approximately 2120 cm^{-1} was linked to C≡C stretching modes or residual organic functional groups introduced by the *C. grandis* extract employed during the green synthesis. The broad band observed at approximately 3500 cm^{-1} was associated with O–H stretching vibrations, confirming the presence of surface hydroxyl groups as well as surface-adsorbed water molecules.

The presence of strong and distinct peaks observed in the FTIR spectra, as well as additional absorption bands, indicated the presence of phytochemical components in the leaf extract of *C. grandis*, including flavonoids, tannins, and polyphenols possessing functional groups such as hydroxyl and carbonyl groups. These phytochemicals served as reducing, capping, and stabilizing agents during the synthesis.

Additionally, in the case of the rGO–NiS composite, a change was observed in peak position and intensity when compared with isolated rGO, which was mainly attributed to the reduction of bands related to oxygen-containing groups and the emergence of the Ni–S stretching vibration. The FTIR spectral features suggested possible interfacial interaction between NiS nanoparticles and rGO sheets. The remaining phytochemical functional groups may be attributed to residual biomolecules from the *C. grandis* leaf extract, which acted as reducing, stabilizing, and capping agents during the synthesis of the nanoparticles.

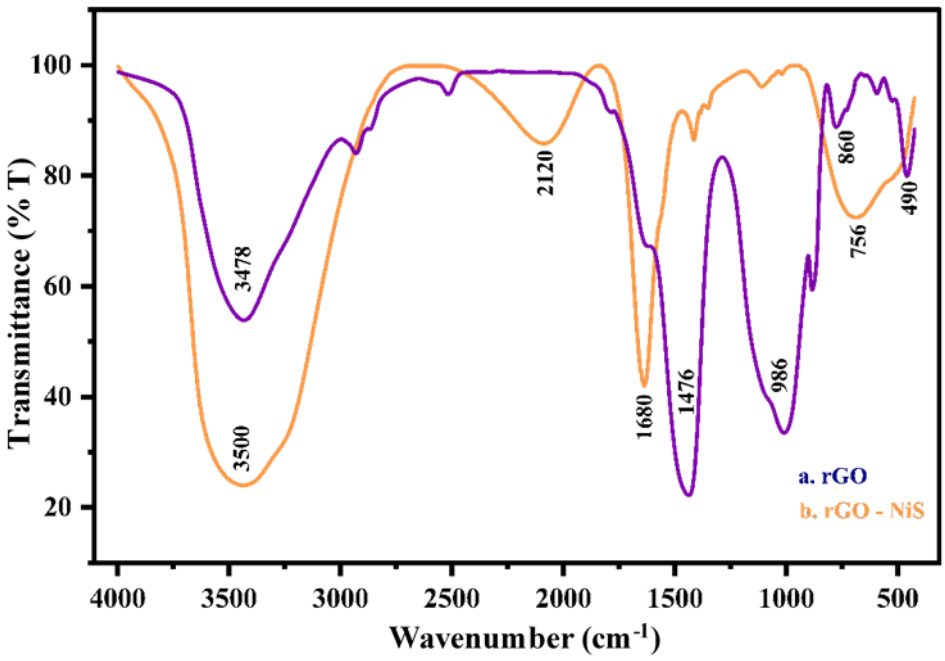

Fig. 5. FTIR spectra of (a) rGO and (b) rGO–NiS nanocomposite

3.3. *Dynamic Light Scattering Analysis*

The DLS analysis of the rGO–NiS nanocomposite (Fig. 6a and 6b) revealed a dominant particle size distribution centered at approximately 100 nm, indicating the formation of nanoscale composite particles exhibiting relatively high uniformity. The particle size determined by DLS (~100 nm) was considerably higher than the crystallite size obtained from XRD analysis (2–5 nm), which is expected because DLS measures the hydrodynamic particle size in suspension, whereas XRD provides the average crystallite size. The autocorrelation function (Fig. 6b) exhibited a smooth decay profile, indicating a relatively uniform particle size distribution and good dispersion stability of the synthesized rGO–NiS nanocomposite. The DLS results indicated relatively improved colloidal dispersion along with reduced particle agglomeration observed under the present synthesis conditions.

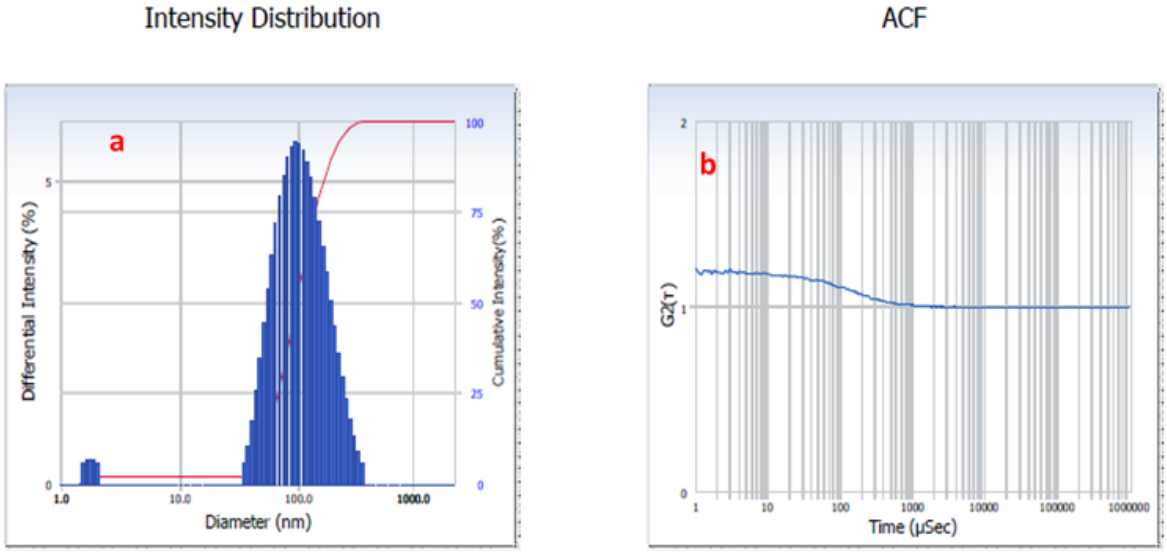

Fig. 6. DLS analysis of rGO–NiS showing (a) particle size distribution and (b) autocorrelation function

3.4. *X-ray diffraction (XRD) analysis*

The X-ray diffraction (XRD) pattern of pure rGO (Fig. 7a) displayed a broad diffraction peak at 2θ ≈ 22.5° in the region of (002) lattice planes, corresponding to enlarged interlayer distances as calculated from Bragg's Law. The diffraction peak exhibited a shift from the (002) lattice planes of graphite at approximately 26.5° (JCPDS card no. 00-041-1487)[24]. This shift indicated effective reduction of GO and the concomitant retention of oxygen functional groups and disordered structures.

The XRD pattern for the rGO–NiS nanocomposite (Fig. 7b) prepared using leaf extract from *C. grandis*, displayed broad diffraction peaks at 2θ ≈ 18.7°, 35.8°, 41.2°, 50.6°, and 58.3°, which were attributed to the (101), (110), (103), (108), and (202) planes of hexagonal NiS (JCPDS card no. 12-0041)[24]. The diffraction peaks corresponding to rGO at approximately 22.5° were observed, whereas the additional diffraction peaks near approximately 26.3° confirmed the reappearance of graphitic ordering.

The enhanced intensity of NiS diffraction peaks relative to those of rGO further suggested that a significant amount of NiS had been effectively loaded onto the surface of the rGO support matrix. The broad and weak diffraction peaks indicated the formation of nanosized NiS and a strong interaction between NiS and rGO sheets.

The average crystallite size of the NiS nanoparticles was estimated using the Debye–Scherrer equation. From the diffraction peak assigned to the (110) plane at $2\theta \approx 35.8°$, the crystallite size of NiS nanocrystallites was determined to be approximately 2–5 nm. The obtained values represented approximate crystallite dimensions since instrumental broadening correction and detailed peak-profile fitting were not performed in the present analysis.

The remaining two diffraction peaks of rGO, situated at $2\theta \approx 22.5°$, were ascribed to a crystallite size of 30.4 nm. This comparison indicated that nanosized NiS particles had formed on the rGO surface.[24]

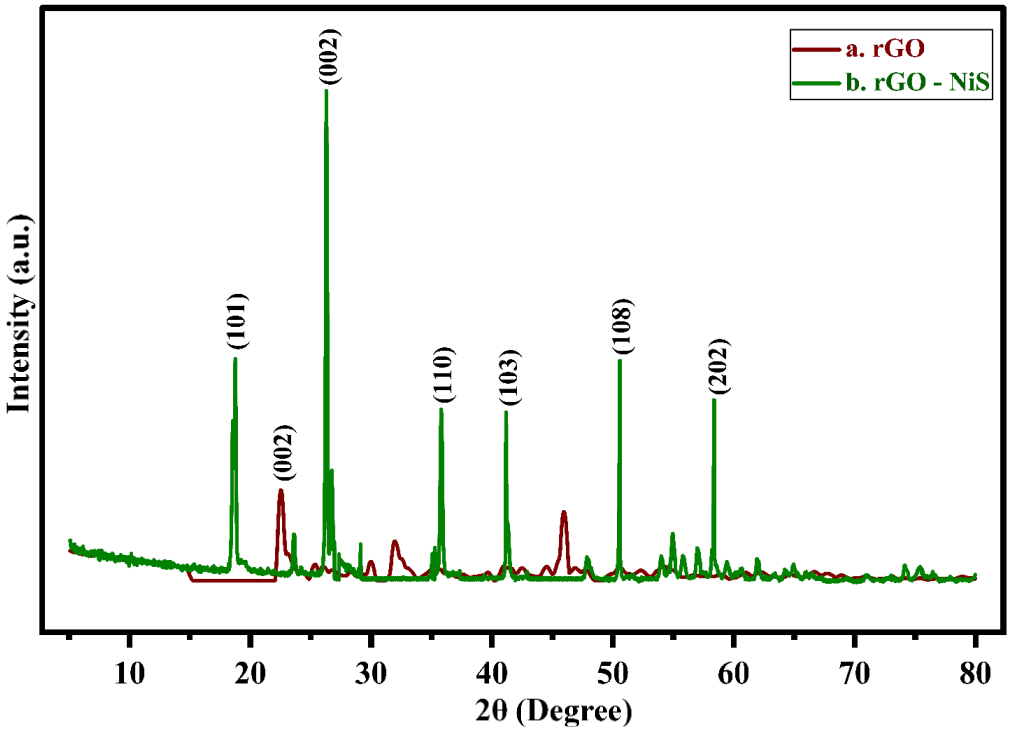

Fig. 7. XRD patterns of (a) rGO and (b) rGO–NiS nanocomposite

3.5. *Morphological and elemental analysis (SEM–EDS)*

From SEM analysis, it was evident that the morphological features of pure NiS and rGO–NiS nanocomposite were noticeably different. Pure NiS shown in Figure 8a exhibited irregularly shaped particles with significant agglomeration and an approximate particle size of approximately 50–200 nm, likely due to the absence of a supporting matrix. In contrast, the rGO–NiS nanocomposite (Fig. 8b) exhibited a sheet-like, wrinkled surface morphology associated with reduced rGO sheets, and NiS particles appeared relatively well distributed over the rGO surface. The particle size of NiS in the composite (~20–80 nm) was comparatively smaller than that of pure NiS, suggesting that the rGO support may have helped suppress excessive particle growth and reduce particle agglomeration during synthesis. These observations suggested that rGO served as an effective conductive supporting framework for the dispersion of NiS nanoparticles.

The wrinkled and interconnected morphology of the rGO sheets was thought to provide conductive pathways for efficient electron transport during electrochemical cycling. In addition, the relatively smaller NiS particles distributed on the rGO surface were believed to increase the electrochemically active surface area and improve electrolyte-ion accessibility. Such structural features were expected to facilitate charge-transfer processes and contribute to the enhanced electrochemical performance of the rGO–NiS electrode.

EDS analysis provided additional evidence of the elemental composition of the synthesized materials. The EDS spectrum of the synthesized NiS sample (Fig. 8a-1) exhibited characteristic signals corresponding to Ni and S, confirming the formation of nickel sulfide. Quantitative EDS analysis revealed Ni as the predominant detected element, while sulfur was present in a comparatively lower amount. The EDS spectrum of the rGO–NiS nanocomposite (Fig. 8b-1) exhibited signals corresponding to Ni, S, and C, confirming the incorporation of NiS nanoparticles onto the rGO framework. The presence of carbon was attributed to the rGO sheets, whereas the sulfur signal supported the formation of nickel sulfide within the composite structure. The EDS results confirmed the presence of the expected elemental constituents without significant detectable impurity signals.

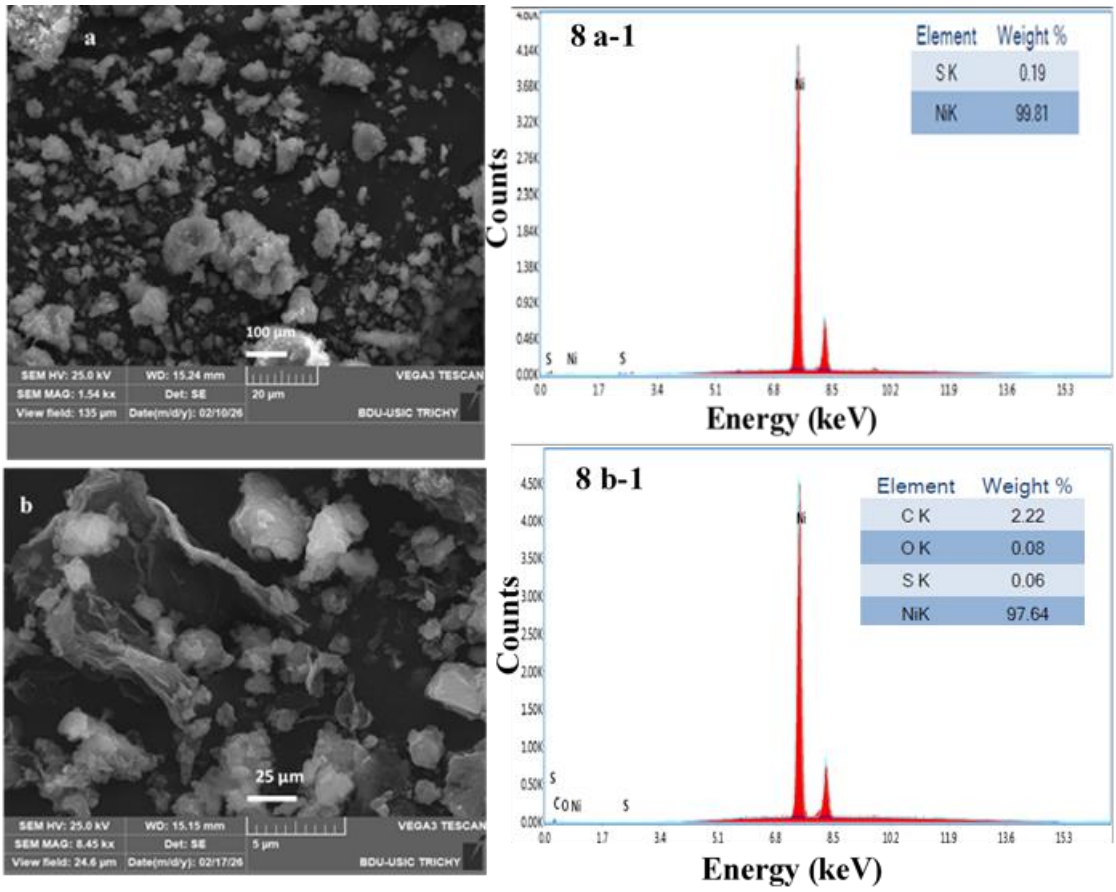

Fig. 8. SEM and EDS images of (a and a-1) NiS nanoparticles and (b and b-1) rGO with NiS

3.6. *Electrochemical performance of rGO–NiS electrode*

The cyclic voltammetry (CV) curves obtained for Ni foam, Ni foam–rGO, and Ni foam–rGO–NiS electrodes in 0.1 M KOH (Fig. 9) clearly demonstrated that electrochemical performance improved with each successive modification. The bare Ni foam electrode displayed a relatively small current response with negligible redox features, indicating predominantly electric double-layer capacitive behavior with limited faradaic contribution. The CV curves for Ni foam–rGO showed an increase in CV area and current response due to improved conductivity and electroactive surface area, with a minor contribution from redox reactions. The CV curves of the Ni foam–rGO–NiS electrode exhibited significantly enhanced current density, along with pronounced anodic and cathodic redox peaks. These results indicated the coexistence of electric double-layer capacitance from conductive rGO sheets and faradaic pseudocapacitance associated with reversible redox reactions of NiS in alkaline electrolyte. The enlarged CV area and distinct redox features suggested improved electrochemical activity and efficient charge-storage behavior, arising from the synergistic interaction between conductive rGO and electroactive NiS nanoparticles.

The pseudocapacitive behavior of the Ni foam–rGO–NiS electrode primarily arose from reversible faradaic redox reactions associated with nickel(II) sulfide species in alkaline electrolyte. During electrochemical cycling, the Ni^{2+} species present in NiS underwent reversible oxidation and reduction processes involving hydroxyl ions (OH^-) from the electrolyte. This redox mechanism was commonly associated with the formation of surface oxyhydroxide intermediates and can be represented by the following reversible reactions:

$$NiS + OH^- \leftrightarrow NiSOH + e^- \quad (2)$$

$$NiSOH + OH^- \leftrightarrow NiSO + H_2O + e^- \quad (3)$$

These reactions corresponded to reversible Ni^{2+}/Ni^{3+} oxidation-state transitions that contributed to the faradaic pseudocapacitive charge-storage behavior of the electrode. Similar electrochemical mechanisms for nickel(II) oxide-based electrodes in alkaline media have been reported previously.[25]

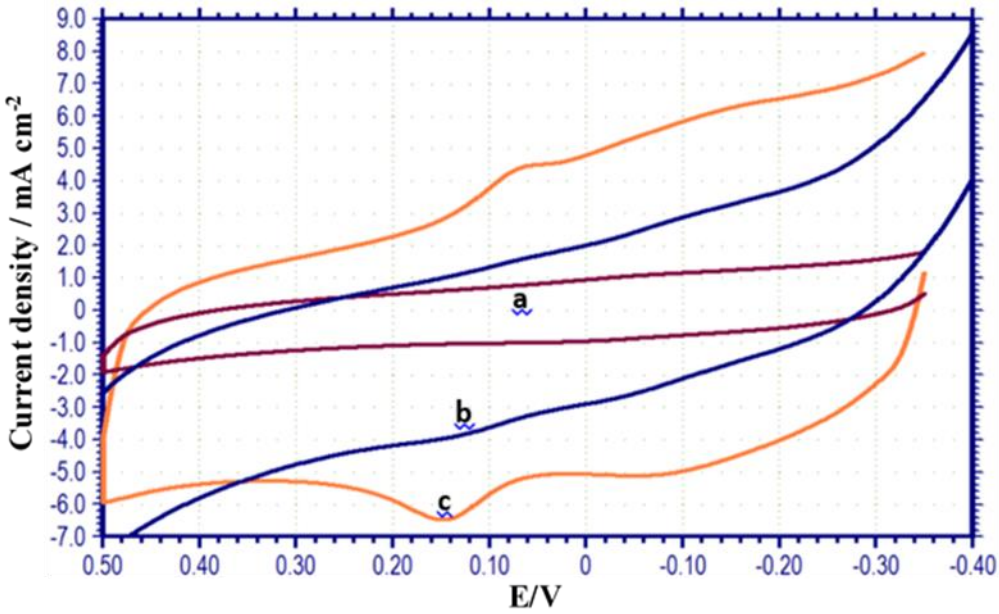

Fig. 9. Cyclic voltammograms of (a) Ni foam, (b) Ni foam–rGO, and (c) Ni foam–rGO–NiS electrodes in 0.1 M KOH

The corresponding Nyquist plots (Fig. 10) revealed clear differences in the electrochemical impedance behavior of the electrodes. The intercept at the real axis in the high-frequency region corresponded to the solution resistance (R_s), while the semi-circular region represented the charge-transfer resistance (R_{ct}) at the electrode/electrolyte interface. Compared with bare Ni foam, the Ni foam–rGO and Ni foam–rGO–NiS electrodes exhibited smaller semicircle diameters, indicating reduced charge-transfer resistance and improved electrical conductivity following the incorporation of conductive rGO and electroactive NiS. Furthermore, the more steeply inclined line observed in the low-frequency region for the Ni foam–rGO–NiS electrode indicated improved ion transport and enhanced capacitive behavior. These results suggested that the combined presence of rGO and NiS contributed to improved electron transport and enhanced electrolyte-ion accessibility within the porous electrode architecture.

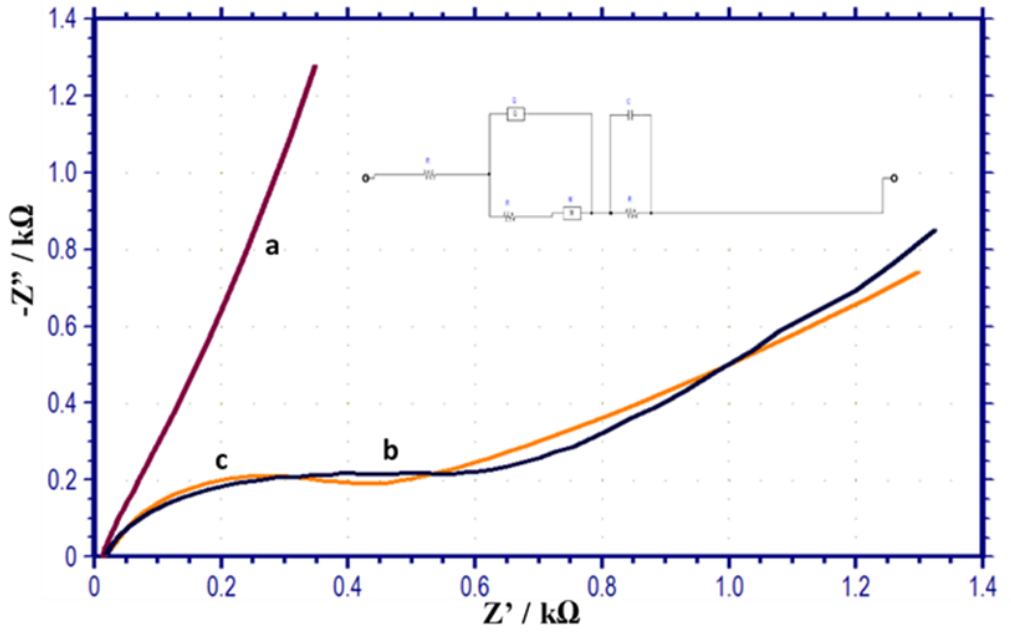

Fig. 10. Electrochemical impedance of (a) Ni foam, (b) Ni foam–rGO, and (c) Ni foam–rGO–NiS electrodes in 0.1 M KOH, with the corresponding equivalent circuit shown in the inset

The variation of the electrochemical response of the Ni foam–rGO and Ni foam–rGO–NiS electrodes with the scan rate in 0.1 M KOH (Fig. 11 and Fig. 12) indicated that both electrodes retained some common charge-storage principles; however, significant differences were predicted in their charge-storage mechanisms and electrochemical kinetics.

The CV curves for the Ni foam–rGO (Fig. 11.a) showed current density increasing with scan rate while maintaining a near-rectangular shape, indicating a predominantly electric double-layer capacitive behavior, supplemented by minor surface redox reactions. The variation of peak current with scan rate provided insight into the charge-storage kinetics of the electrodes.

For the Ni foam–rGO electrode, the approximately linear relationship between peak current and the square root of scan rate ($\nu^{1/2}$) shown in Figure 11.b. Suggested that the electrochemical process involved partial diffusion-controlled ion transport together with surface capacitive contributions. The nearly rectangular CV profile further indicated dominant electric double-layer capacitive behavior associated with the conductive rGO framework.

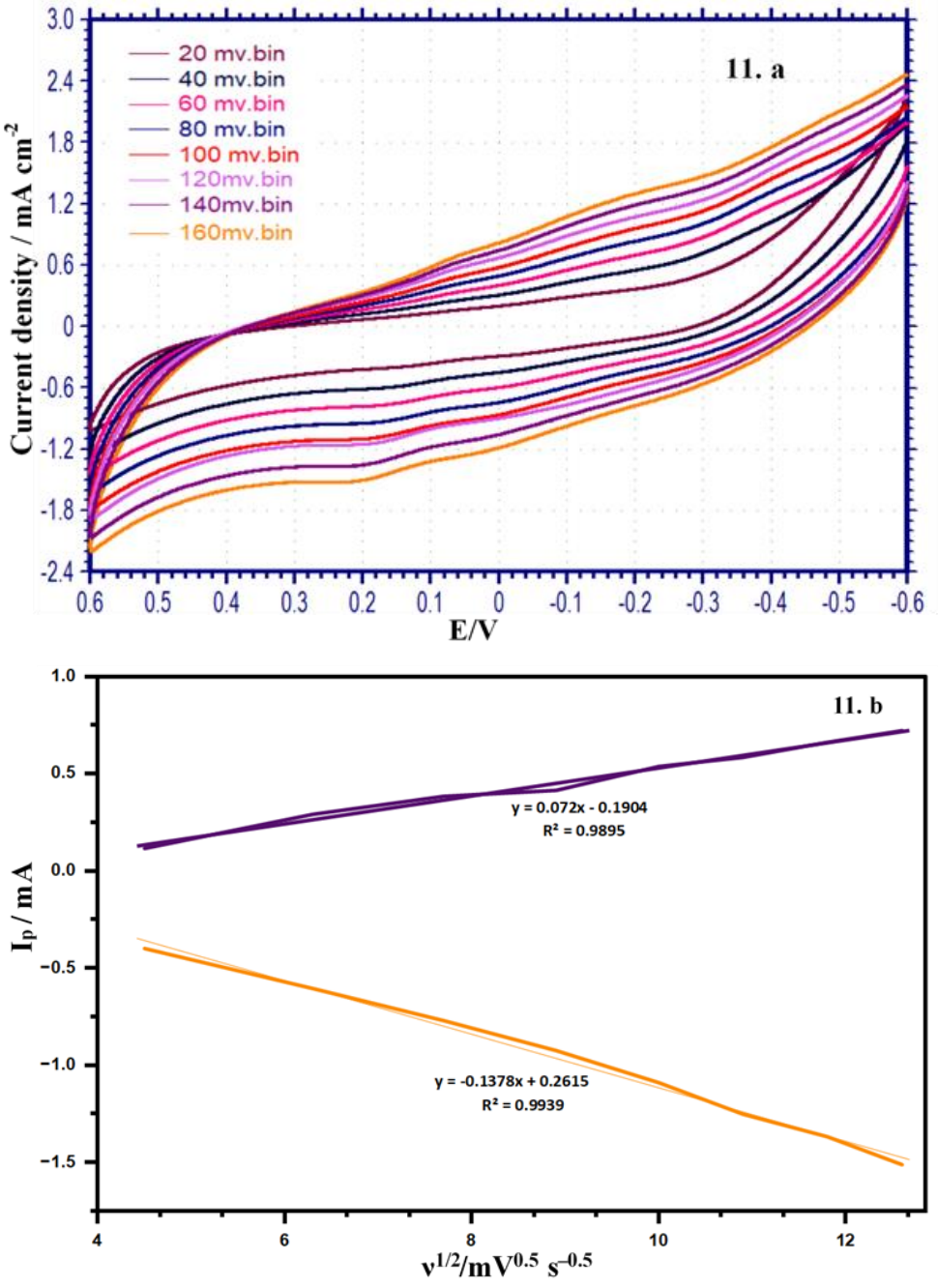

Fig. 11. (a) Scan rate variation of Ni foam–rGO electrode. (b) Linear plots of $\nu^{1/2}/mV^{0.5}\ s^{-0.5}$ versus I_p/mA

In contrast, the Ni foam–rGO–NiS electrode (Fig. 12.a) exhibited significantly enhanced current response together with distinct anodic and cathodic redox peaks, indicating substantial pseudocapacitive contributions originating from reversible faradaic reactions of NiS. The retention of redox characteristics at higher scan rates suggested relatively rapid charge-transfer kinetics and efficient ion diffusion within the electrode structure. Furthermore, the linear relationship between peak current and $v^{1/2}$ observed in Fig. 12.b indicated that the overall charge-storage process involved combined surface capacitive behavior and diffusion-assisted faradaic reactions rather than a purely diffusion-controlled mechanism. The improved electrochemical performance of the Ni foam–rGO–NiS electrode was attributed to the synergistic interaction between conductive rGO sheets, electroactive NiS nanoparticles, and the porous Ni foam substrate, which together facilitated efficient electron transport and electrolyte-ion accessibility.

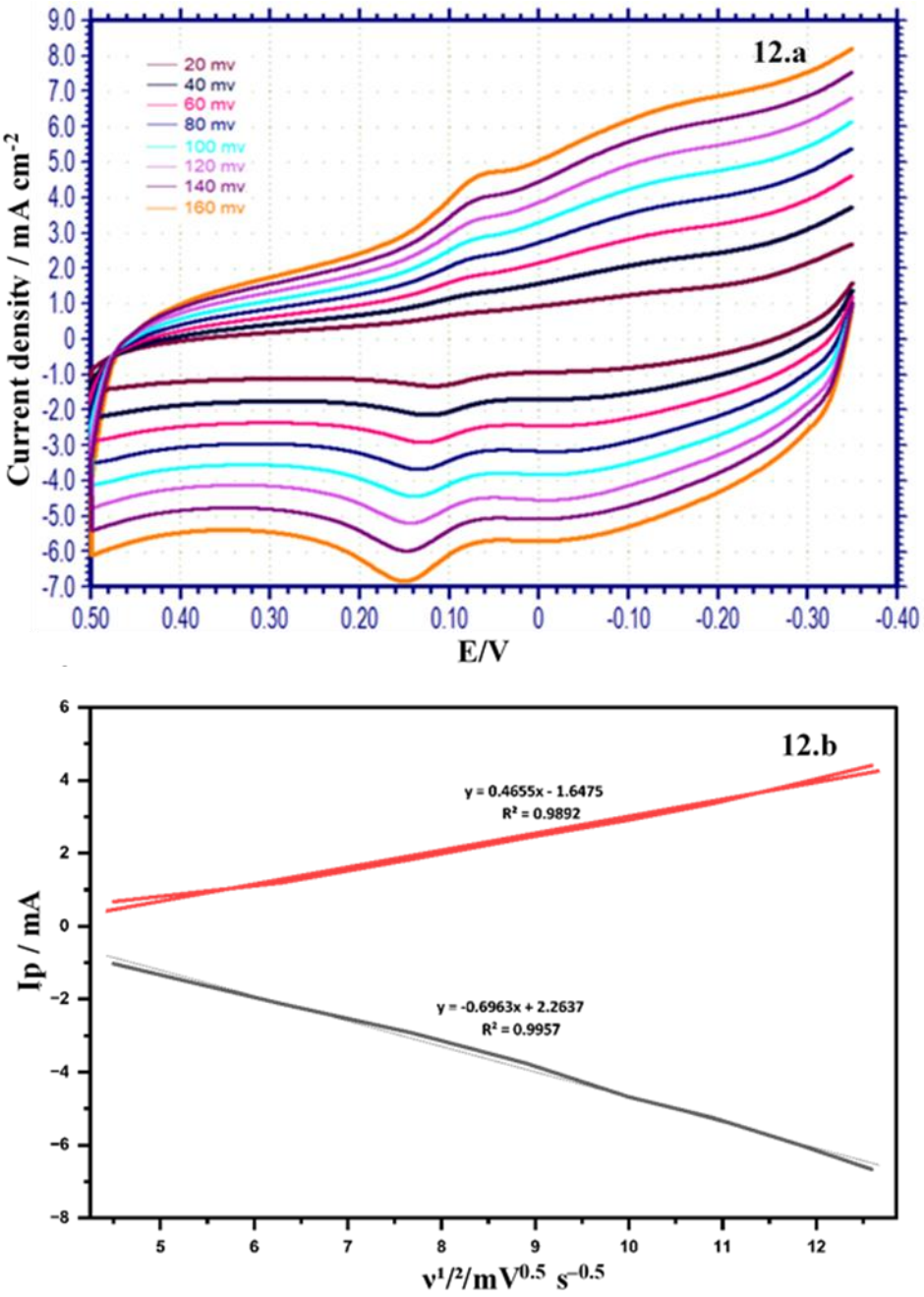

Fig. 12.(a) Scan rate variation of Ni foam–rGO–NiS electrode.
(b) Linear plots of $v^{1/2}/mV^{0.5}\ s^{-0.5}$ versus I_p/mA

The galvanostatic charge–discharge (GCD) profiles of the Ni foam–rGO–NiS electrode at a current density of 1 A g^{-1} (Fig. 13) also exhibited distinctly well-defined, quasi-symmetrical charge–discharge characteristics with a certain deviation from the ideal triangular shape, indicating that pseudocapacitive behavior was dominant due to the faradaic redox reactions. Both the nonlinear potential–time behaviors with the distinct voltage plateaus, and the reversibility of redox reactions corresponding to the nickel-based active species were in good agreement with the faradaic charge-transfer process.

The slight current–resistance drop at the beginning of discharge indicated the low intrinsic resistance of the electrode, thereby facilitating efficient charge transfer through the synergic effect of well-distributed NiS nanoparticles and conductive rGO nanosheets on the surface of Ni foam. Notably, the Ni foam–rGO–NiS electrode possessed a reasonably stable cycling performance, with a capacitance retention of 80–85 % after 3000 cycles, indicating acceptable long-term cycling stability of the electrode material (Fig. 14).

The observed cycling stability was attributed to the structural integrity of the NiS nanoparticles, the conductive rGO framework, and the porous Ni foam substrate, which together facilitated efficient charge transport and helped maintain electrode stability during repeated charge–discharge cycling.

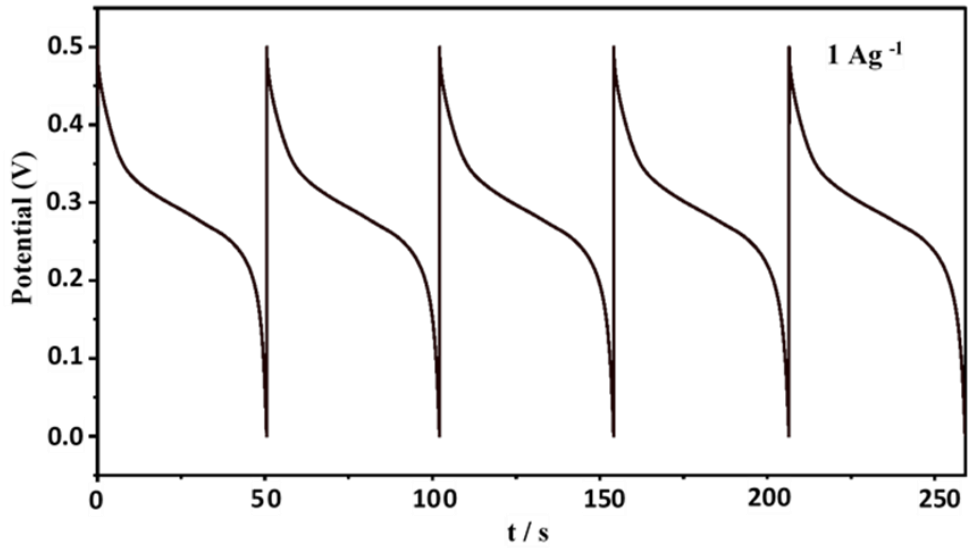

Fig. 13. Galvanostatic charge–discharge (GCD) profiles of the Ni foam–rGO–NiS electrode at a current density of 1 A g^{-1}

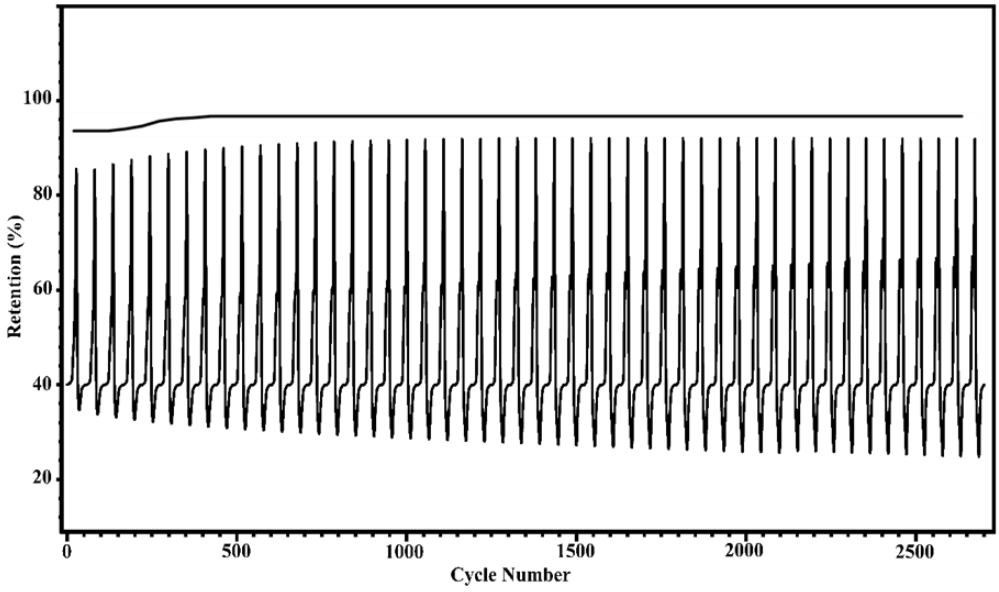

Fig. 14. Cycling performance and capacitance retention of the Ni foam–rGO–NiS electrode over 3000 charge–discharge cycles

The electrochemical performance of the Ni foam–rGO–NiS electrode was also evaluated in terms of galvanostatic charge–discharge (GCD) test curves at different current densities (1–5A g^{-1}), as shown in Figure 15. All the GCD curves displayed a well-defined, nonlinear, quasi-triangular shape with an observable potential plateau, which once again confirmed the pseudocapacitive property of this Ni foam–rGO–NiS electrode. This result was mainly attributed to the electrochemical redox reactions that occurred at the redox-active NiS surface, which also contributed additional capacitance to the overall capacity, while the rGO layer provided a large surface area of electric double-layer capacitance (EDLC). A maximum specific capacitance of 633.3 F g^{-1} was obtained at a current density of 1 A g^{-1}.

The long discharge time period at low current density also demonstrated that most of the active materials had fully reacted, and it provided more time for OH^- ions to permeate deep into the porous structure of the Ni foam to reach the inner surface of the rGO–NiS electrode. When the current density was increased to 5 A g^{-1}, the specific capacitance still remained at a remarkable level (around 422.2 F g^{-1}).[18,26] The incremental decrease in capacitance, however, was very typical at high current density, which resulted from the limited diffusion time of ions and the increased ohmic drop. It was worthy to note that the IR drop was very insignificant between each of the scan lines, which proved that the composite possessed good electrical conductivity and a strong mechanical connection with the Ni foam substrate. The synergistic effect of the highly conducting rGO and the redox-active framework also made the Ni foam–rGO–NiS electrode highly suitable for electrochemical supercapacitor applications.

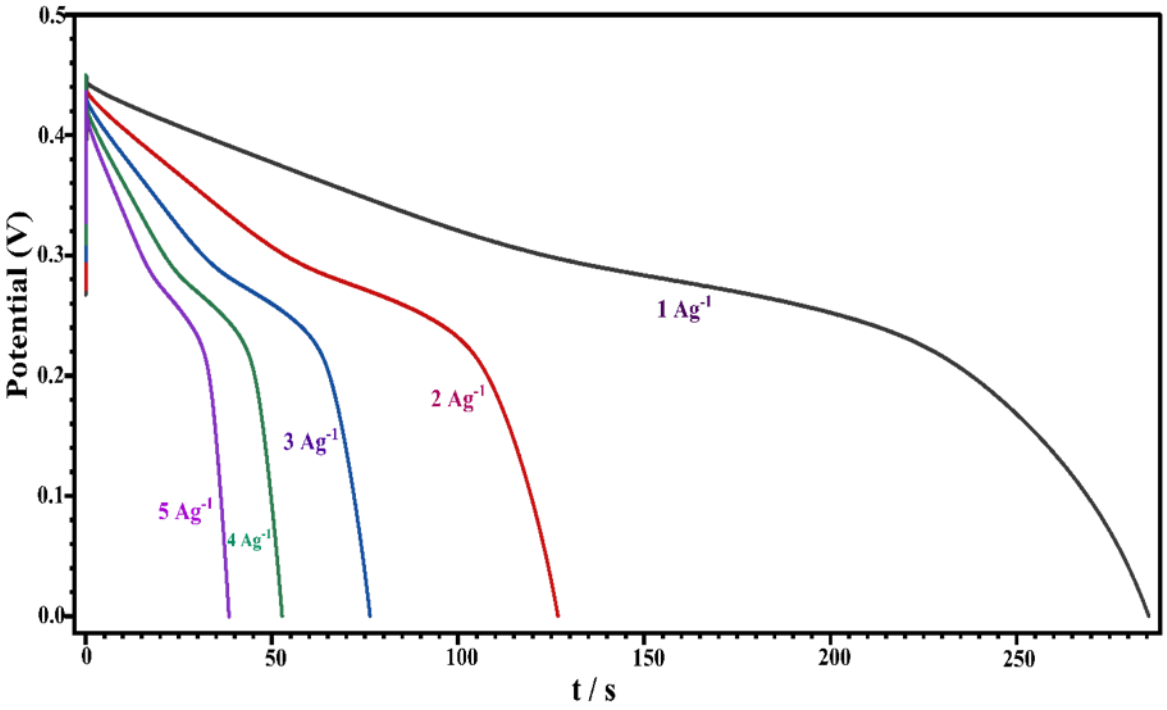

Fig. 15. Galvanostatic charge–discharge (GCD) curves of the Ni foam–rGO–NiS electrode at different current densities ranging from 1 to 5 A g^{-1}

Chronocoulometry (CC) was employed to further assess the charge-storage kinetics and total charge capacity of the Ni foam–rGO–NiS ternary composite (Fig. 16). As indicated by the CC data, the charge accumulated rapidly, peaking at $2.8 \cdot 10^{-4}$ C within a short duration, which demonstrated the high electrochemical activity of the electrode. Additionally, the symmetrical nature of the charge versus time curve indicated a high degree of reversibility in the faradaic redox process. The CC data corroborated the large specific capacitance of 633.3 F g^{-1} and showed that the microwave-assisted fabrication facilitated the diffusion of electrolyte ions and the rapid charge transport across the composite interface.

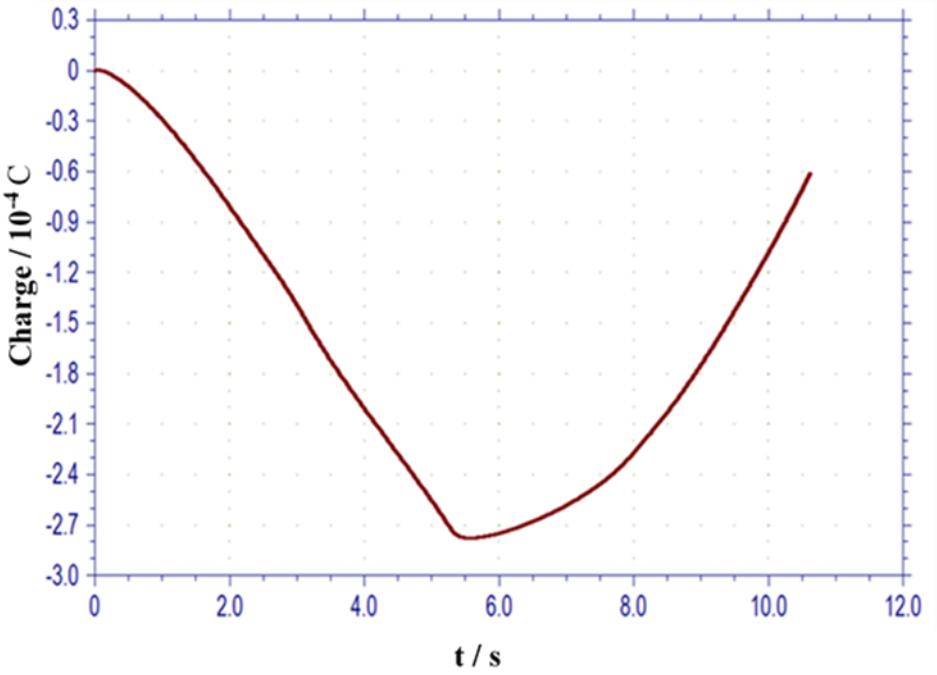

Fig. 16. Chronocoulometric response of the Ni foam–rGO–NiS ternary composite

4. CONCLUSION

In the present work, the rGO–NiS nanocomposite was synthesized using a cost-effective and environmentally benign green synthesis route with the assistance of *C. grandis* leaf extract as a novel reducing agent. The preparation of the rGO–NiS nanocomposite using this sustainable solution represented an advanced strategy for fabricating functional materials for energy storage applications. Structural and spectroscopic analysis unambiguously confirmed the formation of NiS nanoparticles and their uniform decoration onto rGO sheets, along with the presence of interfacial interactions, which enhanced the electronic properties of the material. Morphological characterization revealed that rGO functioned as a conductive substrate, preventing the aggregation of nanoparticles and facilitating their uniform dispersion.

Compared with previously reported chemically synthesized NiS–rGO systems, the present study demonstrated a sustainable, microwave-assisted, bio-mediated fabrication strategy employing *C. grandis* leaf extract as a natural reducing, stabilizing and capping agent. The phytochemical-assisted synthesis facilitated enhanced dispersion of NiS nanoparticles on conductive rGO sheets while suppressing nanoparticle agglomeration. Furthermore, the synergistic integration of conductive rGO pathways, electroactive NiS nanoparticles, and a porous Ni foam substrate contributed to superior electrochemical kinetics and enhanced charge-storage behavior.

Electrochemical tests revealed that superior electrochemical performance of the Ni foam–rGO–NiS electrode was achieved compared with that of bare Ni foam and rGO-modified electrodes. The improvement in specific capacitance, rate capability, low charge-transfer resistance, and acceptable cycling stability was attributed to the synergistic effects of the conductive rGO network, electroactive NiS nanoparticles, and the high-surface-area porous Ni foam substrate. A combination of the electric double-layer capacitance and faradaic pseudocapacitance enabled an electrochemically efficient storage of charge as well as fast ion and electron transport.

In conclusion, the green-synthesized Ni foam–rGO–NiS nanocomposite represented a favorable electrode material for high-performance supercapacitors. This study not only emphasized the significance of a bio-mediated route of synthesis but also provided guidance for preparing inexpensive, environmentally friendly, and highly efficient nanostructured materials for next-generation energy storage devices.

Acknowledgements. We thank Cauvery College for Women (Autonomous) Tiruchirappalli for the financial support under the scheme of DST-CURIE Core grant for Women PG colleges [Reference No. DST/CURIE-PG/2022/8 (G)].

Conflict of interest statement. The authors declare that they have no conflict of interest.

REFERENCES

1. Simon, P.; Gogotsi, Y. Materials for electrochemical capacitors. *Nat. Mater.* **2008**, *7*, 845–854. https://doi.org/10.1038/nmat2297
2. Miller, J. R.; Simon, P. Electrochemical capacitors for energy management. *Science* **2008**, *321*, 651–652. https://doi/10.1126/science.1158736
3. Winter, M.; Brodd, R. J. What are batteries, fuel cells, and supercapacitors? *Chem. Rev.* **2004**, *104*, 4245–4269. https://doi.org/10.1021/cr040110e
4. Antony Sakthi, S.; Priyadarshini, K.; Mani, C.; Rusho Robin Prasad, S.; Dominic, A. Synthesis and characterization of NiCo2S4-MOF-ZIF-67@rGO for efficient electrochemical energy storage. *J. Phys.: Conf. Ser.* **2024**, *2801*, 012001. https://doi.org/10.1088/1742-6596/2801/1/012001
5. Sankari P.; Sivasankari, G.; Kannagi, K.; Pavithra , N.; et al. Study of structural and spectroscopic characterization of ZnS nanoparticles and its application as supercapacitor. *Mod. Phys. Lett. B* **2023**, *37*, 2350150. https://doi.org/10.1142/S0217984923501506
6. Liu, C.; Li, F.; Ma, L. P.; Cheng, H. M. Advanced materials for energy storage. *Adv. Mater.* **2010**, *22*, E28–E62. https://doi.org/10.1002/adma.200903328
7. Antony Sakthi, S.; Rakini Chanderasekaran, J. H.; Niresha Gnana Mary, A.; Surendra Varma, M.; Lakhsmi Prabha, P. Synthesis and characterization of 3D MnNi2O4@MnNi2S4/NF-MOF-67-rGO nanoflower@ nanosheet for ultra-high capacity electrode material. *J. Phys.: Conf. Ser.* **2024**, *2801*, 012009. https://doi.org/10.1088/1742-6596/2801/1/012009
8. Antony Sakthi, S.; Priyadarshini, K.; Mani, C.; Rusho Robin Prasad, S. Synthesis and spectral characterization of high-performance supercapacitor ZIF-67@RGO nanocomposite electrode materials. *Rasayan J. Chem.* **2023**, *16*, 1462–1472. http://doi.org/10.31788/RJC.2023.1638206
9. Conway, B. E. *Electrochemical Supercapacitors: Scientific Fundamentals and Technological Applications*; Springer: New York, NY, USA, 1999. https://doi.org/10.1007/978-1-4757-3058-6
10. Rishav K. Baranwal, Nisantika Biswas, Buddhadeb Oraon, Gautam Majumdar, Advances in Surface Engineering for Improved Energy Storage, *Encyclopedia of Renewable and Sustainable Materials*, Elsevier, **2020**, 245–249, ISBN 9780128131961. https://doi.org/10.1016/B978-0-12-803581-8.11053-7.
11. Augustyn, V.; Simon, P.; Dunn, B. Pseudocapacitive oxide materials for high-rate electrochemical energy storage. *Energy Environ. Sci.* **2014**, *7*, 1597–1614. https://doi.org/10.1039/C3EE44164D
12. Simon, P.; Gogotsi, Y.; Dunn, B. Where do batteries end and supercapacitors begin? *Science* **2014**, *343*, 1210–1211. http://dx.doi.org/10.1126/science.1249625
13. Novoselov, K. S.; et al. A roadmap for graphene. *Nature* **2012**, *490*, 192–200. https://doi.org/10.1038/nature11458
14. Zhu, Y.; Murali, S.; Cai, W.; et al. Graphene and graphene oxide: Synthesis, properties, and applications. *Adv. Mater.* **2010**, *22*, 3906–3924. https://doi.org/10.1002/adma.201001068
15. Dreyer, D. R.; Park, S.; Bielawski, C. W.; Ruoff, R. S. The chemistry of graphene oxide. *Chem. Soc. Rev.* **2010**, *39*, 228–240. https://doi.org/10.1039/B917103G
16. Zheng, M.; Xiao, X.; Li, L.; et al. Hierarchically nanostructured transition metal oxides for supercapacitors. *Sci. China Mater.* **2018**, *61*, 185–209. https://doi.org/10.1007/s40843-017-9095-4
17. Wang, X.; Liu, X.; Rong, H.; et al. Layered manganese-based metal–organic framework as a high capacity electrode material for supercapacitors. *RSC Adv.* **2017**, *7*, 29611–29617. https://doi.org/10.1039/C7RA04374K
18. Wang, H.; Casalongue, H. S.; Liang, Y.; Dai, H. $Ni(OH)_2$ nanoplates grown on graphene as advanced electrochemical pseudocapacitor materials. *J. Am. Chem. Soc.* **2010**, *132*, 7472–7477. https://doi.org/10.1021/ja102267j
19. Yan, J.; Wang, Q.; Wei, T.; Fan, Z. Recent advances in design and fabrication of electrochemical supercapacitors with high energy densities. *Adv. Energy Mater.* **2013**, *4*, 1300816. https://doi.org/10.1002/aenm.201300816
20. Iravani, S. Green synthesis of metal nanoparticles using plants. *Green Chem.* **2011**, *13*, 2638–2650. https://doi.org/10.1039/C1GC15386B
21. Lee, Y.; Joo, N. Identification and quantification of key phytochemicals, phytohormones, and antioxidant properties in *Coccinia grandis* during fruit ripening. *Antioxidants* **2022**, *11*, 2218. https://doi.org/10.3390/antiox11112218
22. Raj, R. A.; AlSalhi, M. S.; Devanesan, S. Microwave-assisted synthesis of nickel oxide nanoparticles using *Coriandrum sativum* leaf extract. *Materials* **2017**, *10*, 460. https://doi.org/10.3390/ma10050460
23. Marcano, D. C.; Kosynkin, D. V.; Berlin, J. M.; Sinitskii, A.; Sun, Z.; Slesarev, A.; Alemany, L. B.; Lu, W.; Tour, J. M. Improved synthesis of graphene oxide. ACS Nano 2010, 4, 4806–4814. https://doi.org/10.1021/nn1006368
24. Cullity, B. D. *Elements of X-Ray Diffraction*, 2nd ed.; Addison-Wesley Publishing Company Inc.: Reading, MA, USA, **1978**. ISBN 0-201-01174-3.
25. Soheila F.: Farid N A, Microwave-assisted synthesis of metal oxide/hydroxide composite electrodes for high power supercapacitors - A review. *J. of. Pow. Sou.* **2014**, 263, 338–360. https://doi.org/10.1016/j.jpowsour.2014.03.144
26. Wang, G.; Zhang, L.; Zhang, J. A review of electrode materials for electrochemical supercapacitors. *Chem. Soc. Rev.* **2012**, *41*, 797–828. https://doi.org/10.1039/C1CS15060J